Research Article

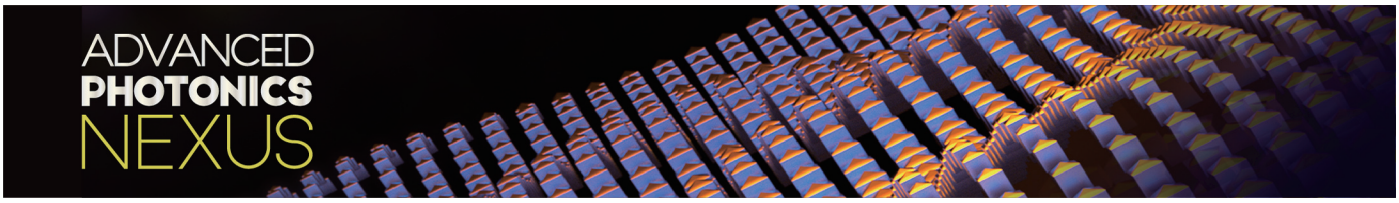

Dynamic multifunctional all-chalcogenide metasurface filter with ultra-multiple cycles

Mingjie Zhang,[a,*,†] Zhanbo Wen,[a,†] Zhenqi Huang,[a,†] Yuanzhi Chen,[b,*] Minsi Lin,[a] Yue Shen,[a] Yan Li,[c] Shunyu Yao,[c] Zhen Li,[a] Zhenqiang Chen,[a] and Zhaohui Li[c]

[a]Jinan University, College of Physics and Optoelectronic Engineering, Guangzhou, China
[b]Shanghai Institute of Technology, School of Material Science and Engineering, Shanghai, China
[c]Sun Yat-sen University, School of Electrical and Information Technology, Guangzhou, China

Abstract. Dynamically tunable metasurfaces employing chalcogenide phase-change materials (PCMs) such as $Ge_2Sb_2Te_5$ alloys have garnered significant attention and research efforts. However, the utilization of chalcogenide PCMs in dynamic metasurface devices necessitates protection, owing to their susceptibility to volatilization and oxidation. Conventional protective layer materials such as Al_2O_3, TiO_2, and SiO_2 present potential drawbacks including diffusion, oxidation, or thermal expansion coefficient mismatch with chalcogenide PCMs during high-temperature phase transition, severely limiting the durability of chalcogenide PCM-based devices. In this paper, we propose, for the first time to our knowledge, the utilization of chalcogenide glass characterized by high thermal stability as a protective material for chalcogenide PCM. This approach addresses the durability challenge of current dynamic photonic devices based on chalcogenide PCM by virtue of their closely matched optical and thermal properties. Building upon this innovation, we introduce an all-chalcogenide dynamic tunable metasurface filter and comprehensively simulate and analyze its characteristics. This pioneering work paves the way for the design and practical implementation of optically dynamically tunable metasurface devices leveraging chalcogenide PCMs, ushering in new opportunities in the field.

Keywords: metasurface; chalcogenide glass; $Ge_2Sb_2Te_5$; phase-change materials.

Received Mar. 29, 2024; revised manuscript received Jun. 9, 2024; accepted for publication Jul. 8, 2024; published online Jul. 31, 2024.

[DOI: 10.1117/1.APN.3.5.056012]

1 Introduction

Metasurfaces, artificially engineered planar structures composed of subwavelength-resonant meta-atoms, have garnered considerable attention owing to their versatile wavefront shaping capabilities.[1–4] Various innovative photonic devices have been developed based on optical metasurfaces, including absorbers,[5–8] planar lenses,[9,10] polarizers,[11,12] beam diverters,[13,14] and holograms,[15,16] among others. In these devices, subwavelength meta-atoms play a crucial role in locally engineering the phase, amplitude, and polarization of light, leveraging their ability to support electrical and/or magnetic resonances. Typically crafted from materials such as metal or dielectrics such as gold, silicon, and germanium, these meta-atoms confer fixed functionality to metasurfaces, with their optical response predetermined by their structure, size, spatial arrangement, and material properties,[3] thereby constraining their applications to some extent. Reconfigurable metasurfaces, endowed with tunable optical responses, present exciting prospects for wavefront shaping, offering broader utility than conventional optical metasurfaces.[17,18] Dynamic metasurfaces achieve this versatility by manipulating the optical properties of the active material comprising the meta-atoms. Currently, a range of materials, including transparent conductive oxides,[19,20] semiconductors,[21,22] two-dimensional materials,[23,24] liquid crystals,[25–27] and phase-change materials (PCMs)[28–31] have been employed as active constituents for fabricating reconfigurable metasurfaces, facilitating dynamic wavefront shaping of light. Among these, PCMs have

*Address all correspondence to Mingjie Zhang, mjzhang@jnu.edu.cn; Yuanzhi Chen, yzchen@sit.edu.cn

†These authors contributed equally to this work.

attracted significant attention and extensive research interest due to their distinctive light-modulation capabilities. In particular, chalcogenide PCMs, such as GeSbTe-based alloys, exhibit rapid and reversible switching between amorphous and crystalline states under external stimuli such as thermal, optical, or electrical inputs.[32] This large optical contrast offers substantial flexibility for dynamic wavefront-shaping designs. Notably, unlike other PCMs such as VO_2,[33,34] chalcogenide PCMs are nonvolatile,[35] obviating the need for continuous energy supply to maintain their amorphous or crystalline states. This characteristic enables the realization of fast, energy-efficient dynamically reconfigurable optical metasurfaces and devices. Several metasurfaces incorporating chalcogenide PCMs in the meta-atoms, or even entirely fabricated from chalcogenide PCMs, have been reported. However, the latter configuration, owing to the larger volume of PCM, poses challenges to achieving the high cooling rates required for rapid re-amorphization,[36,37] thereby affecting the switching speed of optical resonances. Regardless of configuration, chalcogenide PCMs necessitate a protective layer to prevent oxidation or volatilization during the phase change process, given the relatively high temperatures involved. Commonly employed protective materials include oxide materials such as Al_2O_3, TiO_2, and SiO_2.[38,39] Furthermore, for designing and fabricating plasmonic-based dynamic metasurfaces, chalcogenide PCMs typically require direct contact with metallic materials such as Au, Ag, or Al, as the plasmonic effect decays exponentially with the distance between the metal layer and the PCM.[40] However, both the oxide protective layer and the metal layer are prone to interfacial reactions or diffusion with chalcogenide PCMs during phase change, affecting the crystallization kinetics and optical constants of the PCMs. Regrettably, many research works have overlooked these issues, resulting in dynamic optical metasurfaces and devices with uncertain switching responses and insufficient cycling times, limited to only tens to hundreds of cycles, which is far below the inherent cycling durability of the materials themselves [$\sim 10^{15}$ cycles for $Ge_2Sb_2Te_5$ (GST)]. Addressing these challenges is imperative for realizing the full potential of chalcogenide PCM-based dynamic metasurfaces and advancing their practical applications. In this article, we present a novel all-dielectric dynamically tunable metasurface design, wherein the meta-atoms are crafted entirely from chalcogenide materials, devoid of any oxide or metal components. In this innovative approach, the chalcogenide PCM is encapsulated within another chalcogenide glass material selected for its superior thermal stability. Unlike the chalcogenide PCM, the chosen chalcogenide glass exhibits heightened resilience against structural and optical parameter alterations at temperatures corresponding to the PCM's phase transition. This design circumvents issues such as oxidation and diffusion that previously led to the deactivation or degradation of chalcogenide PCMs, and is thereby anticipated to significantly augment the switching cycle times of dynamic photonic devices reliant on chalcogenide PCMs. Furthermore, we demonstrate the dynamic filtering functionality of this pioneering all-chalcogenide metasurface, facilitating the transition from dual-channel reflection in the E-band and C-band to single-channel reflection solely within the E-band. We meticulously analyze and elucidate the underlying mechanisms driving this dynamic behavior. In addition, we validate the stability of our devised device through numerical simulations encompassing diverse incident angles, polarizations, and manufacturing deviations. Moreover, we showcase and analyze multi-level modulation predicated on the crystallization ratio of chalcogenide PCMs. We posit that this rational design approach will furnish a fresh paradigm for the development of dynamic metasurfaces and devices predicated on chalcogenide PCMs. By substantially enhancing the switching cycle times of such dynamic photonic devices, this methodology holds promise for catalyzing their widespread application across various domains.

2 Materials and Methods

Figure 1 illustrates the configuration of the designed all-chalcogenide dynamic metasurface filter, comprising arrays of meta-atoms composed of $Ge_{25}Sb_{10}S_{65}/Ge_2Sb_2Te_5$ (GSS/GST). GST was selected as the PCM in our design, owing to its enduring thermal stability in the amorphous phase, rapid phase-switching kinetics, extensive cycling capability, and substantial optical contrast between its two phases. These properties have found widespread applications in rewritable optical disk storage technology and nonvolatile electronic memories.[41,42] Indeed, a plethora of tunable photonic devices leveraging GST have been developed and demonstrated, encompassing filters,[43] switches,[44] and metalenses. The choice of GSS stems from its comparatively elevated thermal stability and laser-induced damage threshold,[45] ensuring stability throughout the phase transition of GST stimulated by thermal, optical, or electrical inputs. Furthermore, our group has successfully realized supercontinuum spectroscopy, soliton frequency combs, and Raman lasers utilizing GSS-integrated devices,[45–47] underscoring the material's stability. Moreover, the chemical composition of GSS closely resembles that of GST, mitigating concerns such as PCM degradation induced by elemental diffusion. The utilization of GSS/GST meta-atom arrays offers a promising avenue for dynamic metasurface design, harnessing the robust properties of both materials to achieve reliable and efficient dynamic optical functionalities.

The geometric parameters of the structural units within the metasurface are optimized to achieve a period (Λ) of 940 nm. The GSS cylinder features a height (H) of 345 nm and a radius (R) of 420 nm, as depicted in Fig. 1. Within the GSS column, a nanodisc of GST is embedded, positioned 172.5 nm above the substrate, with a thickness (h) of 30 nm and a radius (r) of 410 nm. This design choice of a thin PCM nanodisc ensures rapid phase-switching capabilities. The refractive index (n) and extinction coefficient (k) of both GSS and GST are presented in Fig. 2. Unlike GSS, GST exhibits two distinct states, amorphous and crystalline, resulting in separate curves for n and k, represented by solid and dashed lines, respectively. The substantial contrast in n (e.g., $\Delta n \approx 1.6$@1550 nm) signifies that resonance modes supported by the array can be tailored by adjusting the crystallinity of GST, thereby enabling wavelength selection.

3 Results and Discussion

To elucidate the independent and reconfigurable control of resonances achieved by the all-chalcogenide metasurface, we devised and numerically simulated a filtering/switching device operating within the E and C telecommunication bands. These simulations were conducted employing the finite-difference time-domain method. Figure 3(a) illustrates the reflectance spectrum (R) of the designed all-chalcogenide metasurface. In the amorphous state of GST (a-GST), the reflection spectrum manifests two distinct, spectrally separated resonances within the E and C telecommunication bands. These resonances arise from the magnetic dipole (MD) and electric dipole (ED) modes

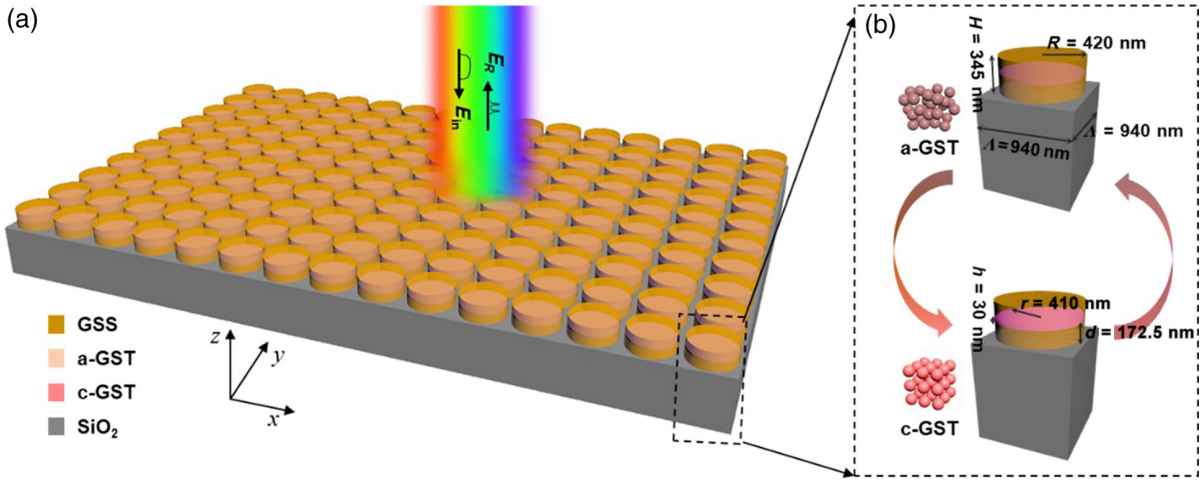

Fig. 1 (a) Schematic depiction of the envisioned all-chalcogenide dynamically tunable metasurface filter. The meta-atom composing the metasurface comprises the highly thermally stable $Ge_{25}Sb_{10}S_{65}$ (GSS) and $Ge_2Sb_2Te_5$ (GST). (b) Illustration of the meta-atom geometry of the proposed metasurface. The period (Λ) of the unit structure is 940 nm; the protective layer GSS has a height (H) of 345 nm and a radius (R) of 420 nm; and a PCM GST with a thickness (h) of 30 nm and a radius (r) of 410 nm is embedded in the GSS and placed at a distance of 172.5 nm above the substrate.

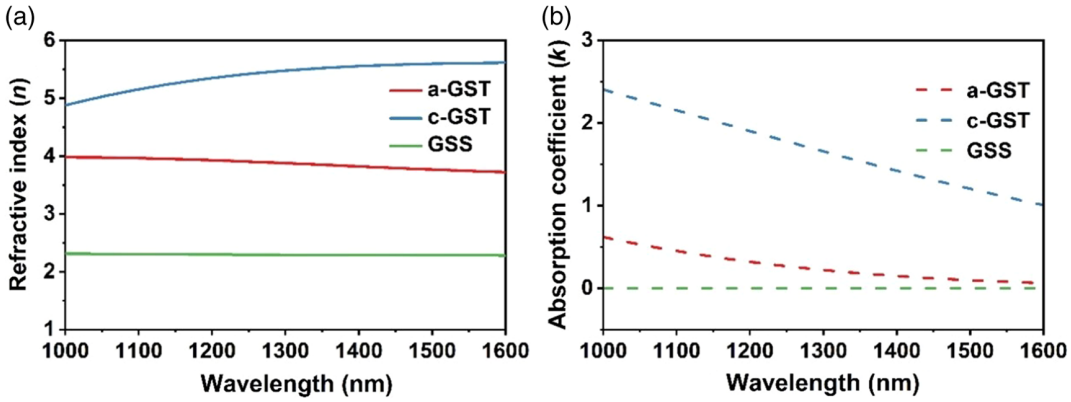

Fig. 2 (a) Refractive indices (n) and (b) absorption coefficients (k) of amorphous GST (a-GST), crystalline GST (c-GST), and GSS glass.

of the single meta-atom, culminating in a dual-band filtering behavior.[32,48] However, when GST transitions to the crystalline state (c-GST), the resonant peak within the C telecommunications band attributable to the ED mode undergoes conspicuous attenuation, whereas the resonant peak within the E telecommunication band attributed to the MD mode remains largely unaffected. This behavior can be elucidated by examining the near-field distribution of all-chalcogenide nanopillars at the resonance frequencies of the MD and ED modes, as depicted in Figs. 3(b)–3(e). Figure 3(b) displays the characteristic magnetic field profile of an electric resonance near 1460 nm when GST is in the amorphous state, revealing a significant enhancement of the magnetic field modulus in proximity to the GST layer. Upon transitioning to the crystalline state, GST still exhibits a pronounced interaction with the magnetic field, as illustrated in Fig. 3(c). However, the enhanced absorption coefficient (k) of crystalline GST at this wavelength weakens the MD resonance intensity, consequently reducing the reflectance. Correspondingly, Figs. 3(d) and 3(e) illustrate the typical electric field distribution of the ED. It can be observed that when GST is in its amorphous state, the electric field mode near GST is enhanced, whereas the mode is significantly weakened when GST is in its crystalline state. The drastic difference in electric field patterns leads to a significant decrease in reflectivity at 1550 nm, with a modulation depth (MDR $= R_a - R_c$) reaching 70%. In summary, by selectively suppressing one resonance mode (ED) while maintaining another (MD), the all-chalcogenide metasurface exhibits a reconfigurable dual-band to single-band spectral filtering capability.

In general, the impact of PCM layer switching on modes within such metasurfaces largely hinges on their precise spatial positioning within the overall resonator structure. This presents a significant challenge during the fabrication process, leading to a sharp decline in fault tolerance. However, in the case of our

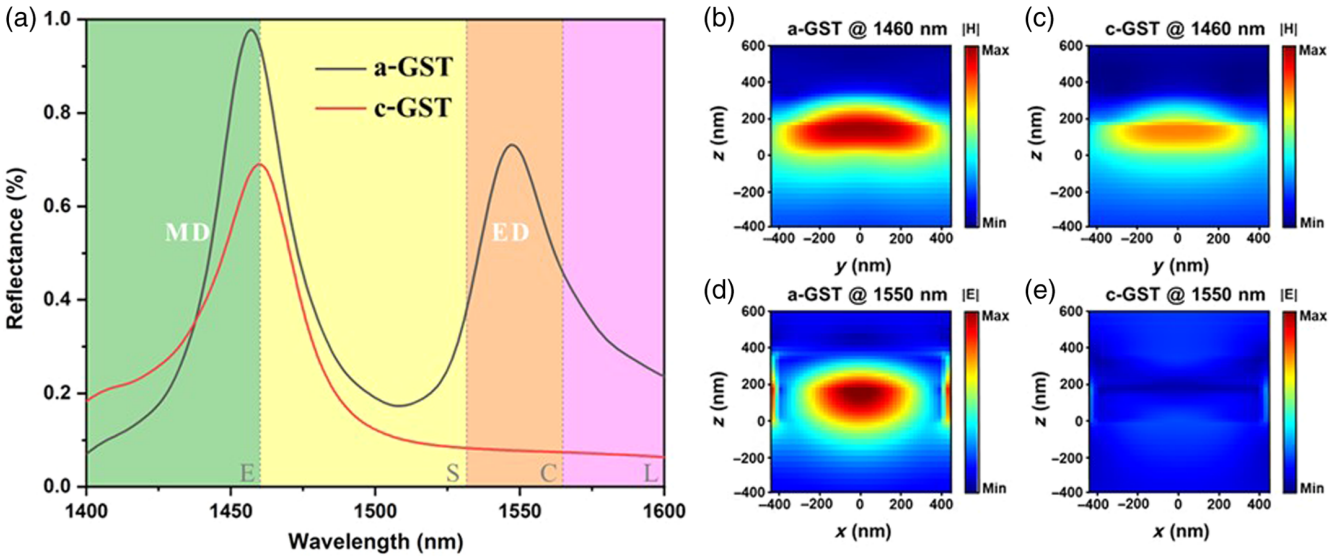

Fig. 3 (a) Reflectance spectra of the designed metasurface under normal incidence conditions, showcasing the distinct responses when GST is in the amorphous (a-GST) and crystalline (c-GST) states. (b) and (c) Magnetic field distributions corresponding to the magnetic resonance of GST in the amorphous and crystalline states, respectively. (d) and (e) Electric field distributions associated with the electric resonance of GST in the amorphous and crystalline states, respectively.

designed all-chalcogenide metasurface, the filtering effect remains relatively stable, even when the center position of GST varies within the range of 150 to 195 nm, as illustrated in Fig. 4. Undoubtedly, this feature confers substantial robustness to the device fabrication process.

Figure 5 depicts the results of a parametric scan evaluating the influence of GST thickness tolerance on device performance. Remarkably, while the resonance peak within the E-band exhibits minimal variation, the resonance peak within the C-band gradually undergoes a redshift with increasing GST thickness. This phenomenon, consistent with the findings from other studies,[49] suggests that the resonant peak in the C-band is more sensitive to the changes in the effective refractive index compared with the resonant peak in the E-band. This sensitivity underscores the importance of precise fabrication processes for the all-chalcogenide metasurface filter. However, this property also offers an opportunity for fine-tuning the filter wavelength within the C-band by controlling the thickness of the GST while maintaining the central position of the E-band unchanged. This ability to selectively adjust the wavelength response within specific bands enhances the versatility and adaptability of the metasurface filter design.

Furthermore, as previously discussed, chalcogenide PCMs can transition between crystalline and amorphous states under electrical, optical, or thermal stimuli, leading to notable alterations in the transmittance, reflectivity, or absorptivity of PCM-based devices. To further refine these changes, the multilevel partially crystalline state of PCM has been achieved by precisely controlling the heating duration or the number of focused ultrashort laser pulses. In this state, the optical and electrical properties of PCM can be finely tuned at multiple levels by adjusting the ratio of crystalline-to-amorphous phases through precise control of the energy of external excitation, thereby enabling multilevel modifications in the performance of PCM-based devices. This capability represents a crucial advantage of chalcogenide PCMs, which finds applications across diverse domains, including multilevel memory, gray-scale images, holograms, and color displays. The effective permittivity corresponding

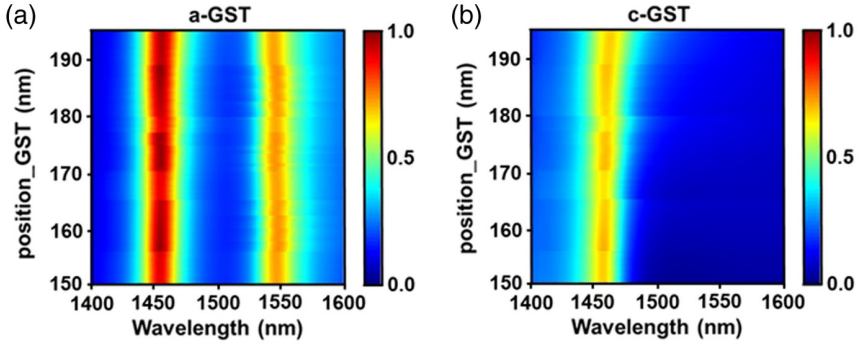

Fig. 4 Relationships between the positions of (a) a-GST and (b) c-GST within the meta-atom of the designed metasurface and the reflection (R) of the metasurface filter, respectively.

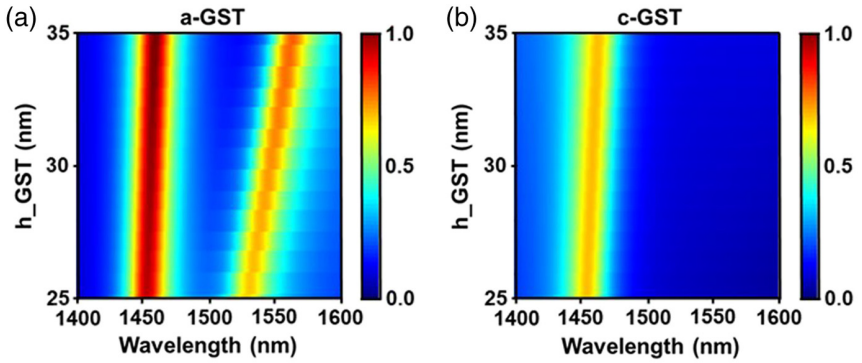

Fig. 5 Relationships between the thicknesses of (a) a-GST and (b) c-GST within the meta-atom of the designed metasurface and the reflection (R) of the metasurface filter, respectively.

to different crystallization rates can be approximated using the effective medium theory and the Lorentz–Lorenz relationship,

$$\frac{\varepsilon_{\text{eff}}(\lambda)-1}{\varepsilon_{\text{eff}}(\lambda)+2}=m\frac{\varepsilon_c(\lambda)-1}{\varepsilon_c(\lambda)+2}+(1-m)\frac{\varepsilon_a(\lambda)-1}{\varepsilon_a(\lambda)+2}. \tag{1}$$

In the presented theories, ε_a and ε_c represent the permittivities of GST in its amorphous and crystalline states, respectively, which are wavelength-dependent. Parameter m denotes the crystallization ratio of GST, varying between 0 (amorphous) and 1 (crystalline). ε_{eff} signifies the permittivity when the crystallization ratio of GST is m.

Building upon these principles, we conducted numerical simulations to investigate the filtering effect of the designed all-chalcogenide metasurface filter on the crystallization ratio m of GST, as depicted in Fig. 6. As shown in the figure, while the position of the reflection peak in the E-band remains relatively unchanged with increasing GST crystallization ratio (m), the reflection peak in the C-band exhibits a significant redshift. This redshift is attributed to the increasing refractive index (n) of GST as the crystallization ratio (m) increases, leading to a shift in the resonance peak position. This observation is further corroborated by the redshift of the resonance peak when the GST thickness is altered, as shown in Fig. 5(a). In addition, this phenomenon indicates that the C-band reflection peak is more sensitive to changes in the effective refractive index of the metasurface. Moreover, it is noteworthy that the intensities of both reflection peaks exhibit a linear decrease as m increases. This behavior can be attributed to the higher extinction coefficient k of c-GST, as illustrated in Fig. 2. Notably, due to the evident shift in the central position of the reflection spectrum within the C-band with changing m, the variation in m exerts a more pronounced impact on the reflection intensity within the E-band. Consequently, the reflection intensity of the E-band can be controlled by adjusting the crystallization ratio m of GST. In essence, our designed all-chalcogenide metasurface filter not only facilitates the transition from dual-channel (E-band and C-band) to single-channel (E-band) filtering but also offers the potential for precise intensity modulation within the single-channel (E-band).

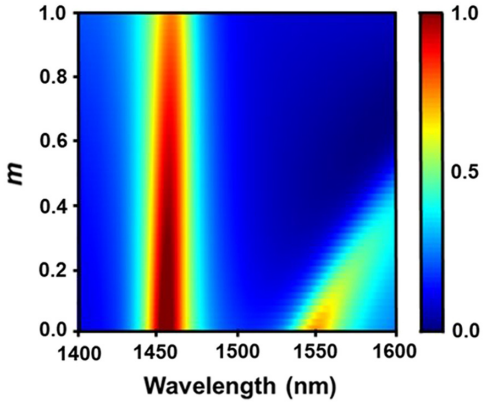

Fig. 6 Reflectivity R of the designed metasurface as a function of GST crystallization ratio m.

All the preceding results have been derived under the assumption of the incident light's electric field direction being along the x axis, corresponding to the transverse magnetic (TM) polarization mode. To delve deeper into the relationship between incident light polarization and filtering characteristics, we conducted a parametric sweep of the electric field direction, where $\phi=0$ deg signifies the TM mode and $\phi=90$ deg represents the transverse electric (TE) polarization mode. The simulation outcomes are illustrated in Fig. 7. Notably, the filter exhibits consistent performance regardless of the changes in polarization angle, demonstrating polarization insensitivity. This observation can be readily understood as the meta-atoms of the metasurface possess circular symmetry within the x–y plane, as depicted in Fig. 1. This circular symmetry ensures that the metasurface's response remains uniform across a range of incident polarization angles.

Unlike the circular symmetry observed in the x–y plane, the meta-atoms of this metasurface exhibit axisymmetry solely in the x–z and y–z planes, as depicted in Fig. 1. Consequently, it is anticipated that changes in incident angle will impact the device performance. To explore this effect, we assessed the robustness of device performance against variations in the incident angle (θ). Specifically, we calculated the reflection for TE and TM polarization states when the incident light deviates by ±5 deg, as presented in Fig. 8. Figures 8(a) and 8(b) depict the angle dependence of the reflectance spectra of a-GST and c-GST under TM excitation, respectively. Notably, akin to observations in Ref. 32, when TM mode incident light interacts with the a-GST metasurface at different angles, the modes associated with ED resonance within the C-band remain relatively stable, suggesting the nonconductivity of this mode. Conversely,

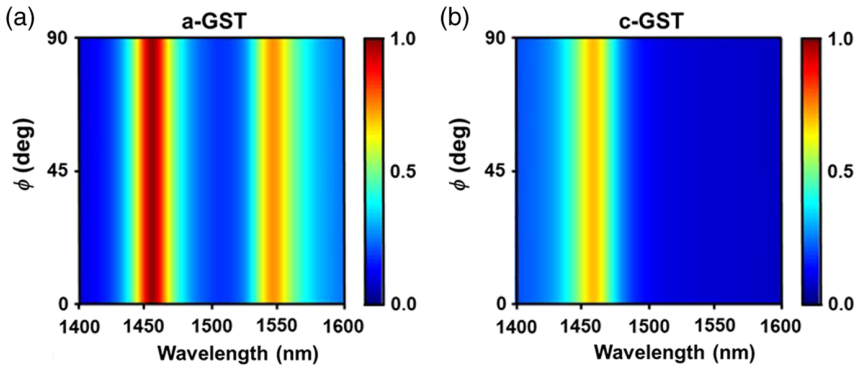

Fig. 7 Relationship between the incident light polarization and the reflection R of the designed metasurface filter for (a) a-GST and (b) c-GST, respectively.

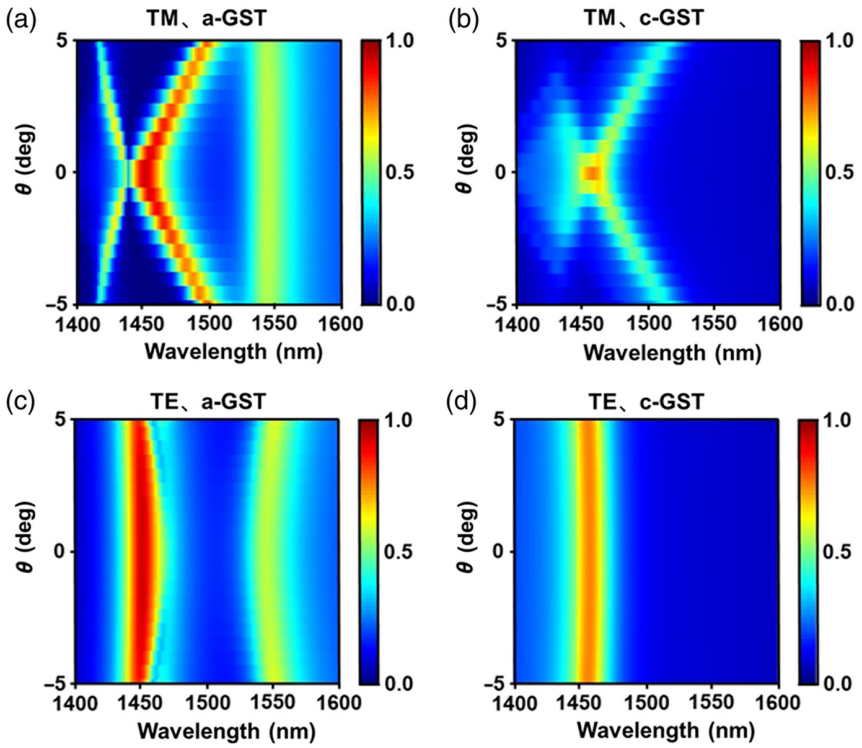

Fig. 8 Relationship between the incidence of TM waves at different angles and the reflection (R) of the designed metasurface filter for (a) a-GST and (b) c-GST, respectively. Relationship between the incidence of TE waves at different angles and the reflection (R) of the designed metasurface filter for (c) a-GST and (d) c-GST, respectively.

the MD correlation mode situated in the E-band splits into two distinct Bloch modes with high dispersion and opposing group velocity signs. Upon transitioning to the crystalline state, the ED-related resonant mode within the C-band disappears, whereas the MD-related resonant mode still bifurcates, albeit with diminished intensities owing to the higher extinction coefficient (k) of c-GST. Conversely, for TE polarization excitation, both ED and MD correlation modes exhibit relatively minor variations under oblique incidence. The device maintains its dual-channel to single-channel filtering characteristics with the phase switching of GST, as illustrated in Figs. 8(c) and 8(d). Leveraging these characteristics, our device can even be utilized to discern the polarization properties of obliquely incident light. Furthermore, the dynamic all-chalcogenide metasurface can achieve multiband filtering of TM-polarized light under oblique incidence.

Here, we introduce a practical phase control scheme, supported by comprehensive photothermal simulations, to validate our assumptions. The thermal simulation model considers the absorption of irradiation light (532 nm) by GST, the thermal conduction between GSS and GST, and the convective heat transfer between GSS and air. Considering the high absorption coefficient of GST at the 532 nm wavelength and the near-transparent nature of GSS at this wavelength, the contribution of

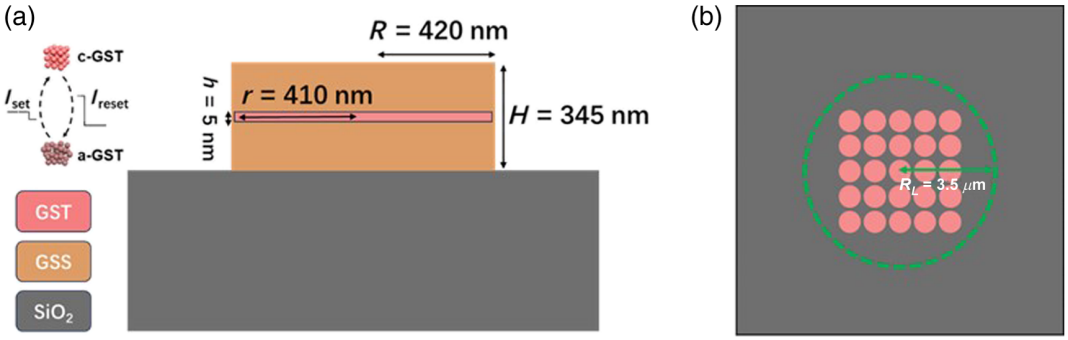

Fig. 9 (a) Illustration of the transversal section of the phase-change metasurface. (b) Schematic representation of the photothermal control scheme for the proposed GST-GSS metasurface consisting of a 5 × 5 array. R_L denotes the radius of the 532 nm top-hat laser beam.

electric and magnetic dipoles (ED and MD) has been omitted. Illustrated in Figs. 9(a) and 9(b), the exemplified PCM metasurface comprises a 5 × 5 array of units. Each unit consists of a central GST enclosed by GSS. To ensure smooth phase-change processes, it is imperative to employ an appropriate laser wavelength. Specifically, the selected wavelength should correspond to a high extinction coefficient for GST and near-transparency for GSS. In this context, we opt for a 532-nm wavelength laser for optical heating simulations. At this wavelength, GSS exhibits transparency, while GST possesses an imaginary part of the refractive index, $k_a = 1.859$ in its amorphous state and $k_c = 2.901$ in its crystalline state. As depicted in the inset of Fig. 9(b), the phase transition process involves heating GST above the crystalline temperature ($T_c = 150$°C) using a long, low-intensity pulse of I_{set} to achieve crystallization. Conversely, the amorphization process entails subjecting GST to a short, high-intensity pulse of I_{reset}, heating it above the melting point ($T_m = 600$°C), followed by rapid cooling below the crystalline temperature. This carefully orchestrated heating strategy ensures precise control over the phase transition of GST within the metasurface structure.

The optical–thermal control of the phase-change metasurface was simulated using COMSOL Multiphysics. We coupled the radiative beam in the absorbing media module with the heat transfer in the solids module to conduct this simulation. The thermal parameters of the materials involved in this simulation are listed in Table 1.

Based on the aforementioned parameters, we simulated the amorphization and crystallization of a single meta-atom using a high-energy pulse with a duration of 5 ns and a low-energy pulse with a duration of 25 ns, respectively. Both pulses are uniform plane waves with a spot radius of 420 nm. To ensure complete phase transitions of GST, the center temperatures during the amorphization and crystallization processes are set at ~650°C and ~180°C, respectively. It is worth mentioning that the temperature of 650°C is higher than the melting temperature of GST. This setting is due to the almost unavoidable temperature gradient of the meta-atom during the heating process, caused by the asymmetric environment around the atoms from the substrate. Only a higher temperature can fully ensure the complete phase transition of GST. As shown in Figs. 10(a) and 10(b), the optical power required to heat to the desired temperatures is 0.5 and 2.2 mW, respectively. This low power consumption is attributed to the high absorption coefficient of GST for 532 nm light and the design of a thin GST layer. Meanwhile, as shown in Fig. 10(b), it only takes 5 ns for GST to cool from the melting temperature to the crystallization temperature. Such a high cooling rate also ensures the amorphization of GST effectively.

Furthermore, by employing the same pulse and simply increasing the spot size [as depicted in Fig. 9(b)], we validated a 5 × 5 metasurface heating using the same approach. Similarly, the power required to heat the amorphization and crystallization processes to the same temperature is 110 and 12 mW, respectively, with the temperature profile shown in Fig. 11(a). Figures 11(b) and 11(c) show the top and side views of the temperature distribution of the 5 × 5 metasurface in the high-temperature state, respectively. The outer meta-atoms exhibit slightly lower temperature distribution compared with the central ones due to better thermal convection conditions at the exterior, which aligns with practical laws. This phenomenon also indirectly reflects the model's rationality and accuracy. However, as the set temperature is slightly higher than the melting and crystallization temperatures of GST, it ensures the complete phase transition of GST. Therefore, we have reason to believe that heating a larger array of all-chalcogenide metasurfaces only requires increasing the spot size and power.

Furthermore, we monitored the temperature of the GSS during the phase transition process to ensure it remains within a safe

Table 1 Thermal properties of materials used in simulations.

	a-GST	c-GST	GSS	SiO_2
Density (kg m^{-3})	6.16	6.25	3.111	2.203
Specific heat (J kg^{-1} K^{-1})	202	202	9700	740
Thermal conductivity (W m^{-1} K^{-1})	0.29	0.42	3.184	1.38
Imaginary part of the refractive index	1.859	2.901	0.0001	0.0001

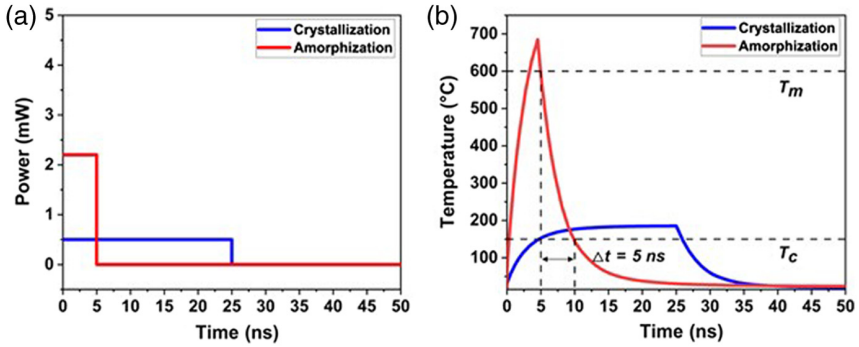

Fig. 10 (a) Power curves depicting the crystallization and amorphization simulation processes of a single unit. (b) Simulated thermal curves of the GST central region of a single unit during the crystallization and amorphization simulation processes.

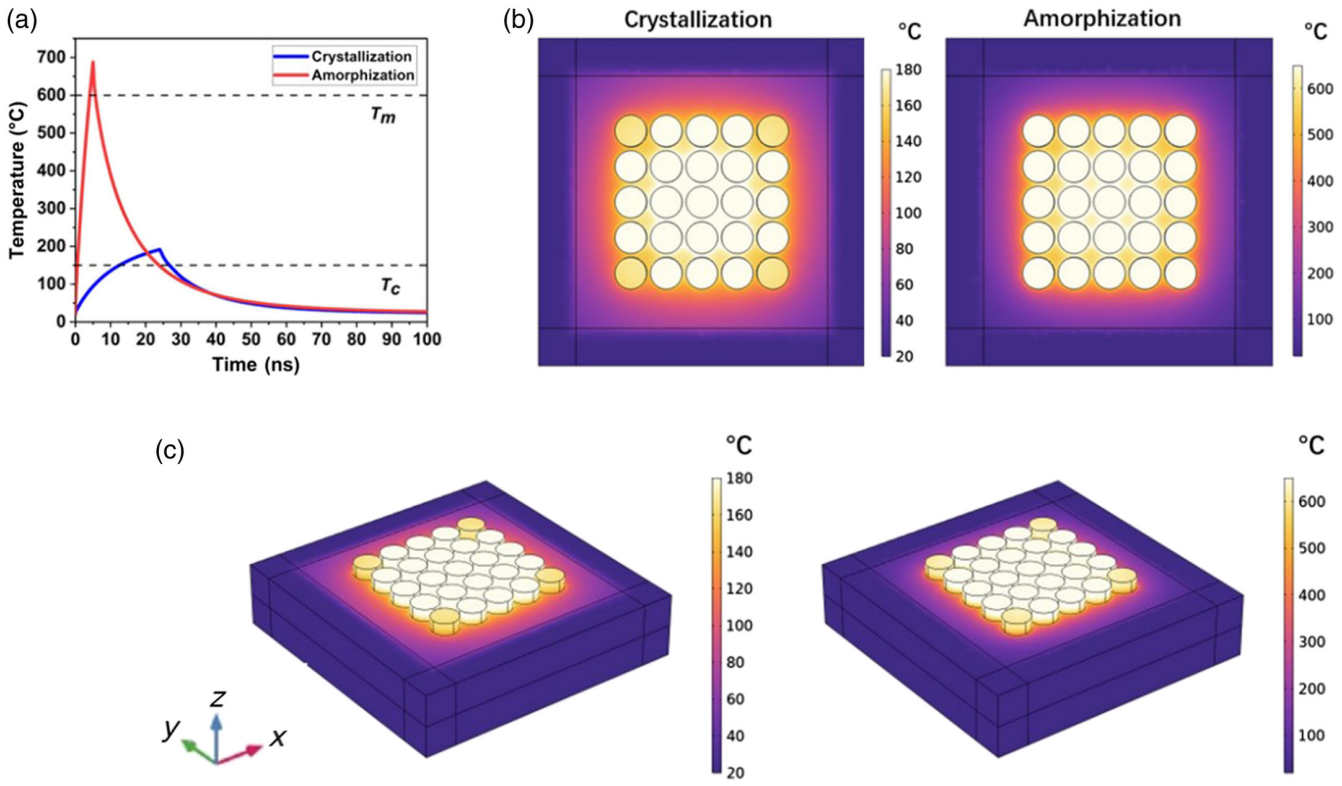

Fig. 11 (a) Calculated average thermal curves of the GST central temperatures for the 5 × 5 metasurface during the crystallization and amorphization simulation processes. (b) Top view and (c) side view of the thermal distribution during the metasurface crystallization and amorphization simulation process.

temperature range, thus protecting the GST. Figures 12(a) and 12(b) show the temperature curves of GSS and GST during the crystallization and amorphization processes of GST, respectively. It can be seen that, regardless of whether GST is crystallizing or amorphizing, the temperature of GSS is almost the same as that of GST, with only a slight increase. Considering the significantly higher thermal stability advantage of GSS compared with GST, GSS can undoubtedly protect GST during its phase transition. The slight temperature difference during the phase transition of GST may be due to the heat conduction speed between GST and GSS being greater than the heat convection speed between GSS and air, rather than the absorption of 532 nm by GSS. To validate this hypothesis, we irradiated the meta-atoms without GST under the same conditions; the temperature variation is shown in Fig. 12(c). The negligible temperature change implies that the 532-nm irradiation light will directly transmit through the GSS without being absorbed or causing resonance of ED and MD. This also confirms the correctness of not considering the resonance of the irradiation light during the GST phase transition process.

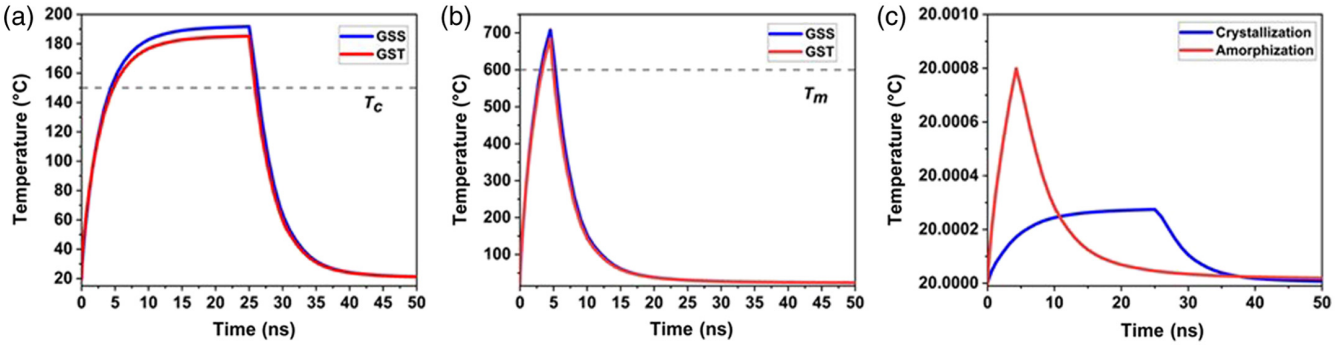

Fig. 12 (a) Simulated thermal curves of a single unit in the crystallization simulation process. (b) Simulated thermal curves of a single unit in the amorphization simulation process. (c) The temperature variation curve for irradiating the GSS meta-atom without GST under the same conditions.

4 Conclusion

In summary, this work addresses the challenge of insufficient durability in current dynamic tunable photonic devices based on chalcogenide PCMs by proposing a novel design approach utilizing chalcogenide materials with high thermal stability, specifically chalcogenide glass, as the protective layer. This solution effectively enhances the switching cycle durability of the devices. Leveraging this approach, we introduce and validate a new all-chalcogenide dynamic metasurface filter capable of transitioning from dual-channel reflection (E-band and C-band) to single-channel filtering with exclusive reflection in the E-band. We thoroughly investigate the filtering mechanism and fabrication tolerance, demonstrating robust performance even under manufacturing deviations. Notably, the metasurface filter exploits the multilevel phase transition of GST to not only achieve dual-channel to single-channel filtering but also enable precise intensity modulation within the single-channel (E-band). Furthermore, the polarization insensitivity of this metasurface enhances its versatility and applicability. However, TM incident light is found to be more sensitive to the incident angle compared with TE light, which presents opportunities for polarization characterization of the incident light. In addition, the dynamic all-chalcogenide metasurface exhibits potential for multi-band filtering of TM-polarized light under oblique incidence. In essence, this thoughtful design scheme coupled with outstanding device performance offers a promising pathway for the development of dynamic metasurface devices based on chalcogenide PCMs, opening doors to practical applications across diverse fields.

Disclosures

The authors declare no conflicts of interest.

Code and Data Availability

Data underlying the results in this paper may be obtained from the authors upon reasonable request.

Author Contributions

This paper was written through the contributions of all authors. All authors have given approval to the final version.

Acknowledgments

This work was supported by the Program of Marine Economy Development Special Fund under Department of Natural Resources of Guangdong Province (Grant No. GDNRC [2023] 23), the National Natural Science Foundation of China (Grant Nos. 62005098 and 61935013), the General Items of Guangzhou Science and Technology Plan Project (PhD Young Scientists and Technologists category) (Grant No. 202201010320), and the Fundamental Research Funds for the Central University (Grant No. 11623415).

References

1. N. Yu et al., "Light propagation with phase discontinuities: generalized laws of reflection and refraction," *Science* **334**(6054), 333–337 (2011).
2. S. Zhuo et al., "Dynamic transmissive metasurface for broadband phase-only modulation based on phase-change materials," *Laser Photonics Rev.* **17**(1), 2200403 (2022).
3. Z. Zhang et al., "Recent advances in reconfigurable metasurfaces: principle and applications," *Nanomaterials* **13**(3), 534 (2023).
4. B.-X. Wang et al., "Design and experimental realization of triple-band electromagnetically induced transparency terahertz metamaterials employing two big-bright modes for sensing applications," *Nanoscale* **15**(45), 18435–18446 (2023).
5. L. Kang, R. P. Jenkins, and D. H. Werner, "Recent progress in active optical metasurfaces," *Adv. Opt. Mater.* **7**(14), 1801813 (2019).
6. H. Jing et al., "An optically transparent flexible metasurface absorber with broadband radar absorption and low infrared emissivity," *J. Phys. D: Appl. Phys.* **56**(11), 115103 (2023).
7. B.-X. Wang et al., "Dielectric-based metamaterials for near-perfect light absorption," *Adv. Funct. Mater.*, 2402068 (2024).
8. B.-X. Wang et al., "Design of multiple-frequency-band terahertz metamaterial absorbers with adjustable absorption peaks using toothed resonator," *Mater. Des.* **225**, 111586 (2023).
9. A. Arbabi and A. Faraon, "Advances in optical metalenses," *Nat. Photonics* **17**(1), 16–25 (2023).
10. J. Yao et al., "Integrated-resonant metadevices: a review," *Adv. Photonics* **5**(2), 024001 (2023).
11. S. Wang et al., "Metasurface-based solid Poincaré sphere polarizer," *Phys. Rev. Lett.* **130**(12), 123801 (2023).
12. A. H. Dorrah et al., "Metasurface optics for on-demand polarization transformations along the optical path," *Nat. Photonics* **15**(4), 287–296 (2021).

13. Q. Zhang et al., "Design of beam deflector, splitters, wave plates and metalens using photonic elements with dielectric metasurface," *Opt. Commun.* **411**, 93–100 (2018).
14. W. Daopeng et al., "All-dielectric metasurface beam deflector at the visible frequencies," *Opto-Electron. Eng.* **44**(1), 103–107 (2017).
15. G. Y. Lee, J. Sung, and B. Lee, "Recent advances in metasurface hologram technologies," *ETRI J.* **41**(1), 10–22 (2019).
16. L. Huang, S. Zhang, and T. Zentgraf, "Metasurface holography: from fundamentals to applications," *Nanophotonics* **7**(6), 1169–1190 (2018).
17. S. V. Makarov et al., "Light-induced tuning and reconfiguration of nanophotonic structures," *Laser Photonics Rev.* **11**(5), 1700108 (2017).
18. A. M. Shaltout, V. M. Shalaev, and M. L. Brongersma, "Spatiotemporal light control with active metasurfaces," *Science* **364**(6441), eaat3100 (2019).
19. A. Forouzmand et al., "A tunable multigate indium-tin-oxide-assisted all-dielectric metasurface," *Adv. Opt. Mater.* **6**(7), 1701275 (2018).
20. J. Park et al., "All-solid-state spatial light modulator with independent phase and amplitude control for three-dimensional LiDAR applications," *Nat. Nanotechnol.* **16**(1), 69–76 (2021).
21. P. C. Wu et al., "Dynamic beam steering with all-dielectric electro-optic III-V multiple-quantum-well metasurfaces," *Nat. Commun.* **10**(1), 3654 (2019).
22. P. P. Iyer et al., "III-V heterojunction platform for electrically reconfigurable dielectric metasurfaces," *ACS Photonics* **6**(6), 1345–1350 (2019).
23. Y. Yao et al., "Electrically tunable metasurface perfect absorbers for ultrathin mid-infrared optical modulators," *Nano Lett.* **14**(11), 6526–6532 (2014).
24. Z. Sun, F. Huang, and Y. Fu, "Graphene-based active metasurface with more than 330° phase tunability operating at mid-infrared spectrum," *Carbon* **173**, 512–520 (2021).
25. C. X. Liu et al., "Programmable manipulations of terahertz beams by transmissive digital coding metasurfaces based on liquid crystals," *Adv. Opt. Mater.* **9**(22), 2100932 (2021).
26. M. Sharma, N. Hendler, and T. Ellenbogen, "Electrically switchable color tags based on active liquid-crystal plasmonic metasurface platform," *Adv. Opt. Mater.* **8**(7), 1901182 (2020).
27. I. Kim et al., "Stimuli-responsive dynamic metaholographic displays with designer liquid crystal modulators," *Adv. Mater.* **32**(50), 2004664 (2020).
28. L. Martin-Monier et al., "Endurance of chalcogenide optical phase change materials: a review," *Opt. Mater. Express* **12**(6), 2145–2167 (2022).
29. X. Chen et al., "Neuromorphic photonic memory devices using ultrafast, non-volatile phase-change materials," *Adv. Mater.* **35**(37), 2203909 (2022).
30. V. Korolev et al., "Tunable high-order harmonic generation in GeSbTe nano-films," *Nanophotonics* (2024).
31. O. M. Kushchenko et al., "All optically switchable active photonics based on the halide perovskite GST platform," *Laser Photonics Rev.* **17**(8), 2200836 (2023).
32. C. Ruiz de Galarreta et al., "Reconfigurable multilevel control of hybrid all-dielectric phase-change metasurfaces," *Optica* **7**(5), 476–484 (2020).
33. X. Lu et al., "Two-channel VO_2 memory meta-device for terahertz waves," *Nanomaterials* **11**(12), 3409 (2021).
34. F. Ding, S. Zhong, and S. I. Bozhevolnyi, "Vanadium dioxide integrated metasurfaces with switchable functionalities at terahertz frequencies," *Adv. Opt. Mater.* **6**(9), 1701204 (2018).
35. A. Solomonov et al., "Ge-Sb-Te based metasurface with angle-tunable switchable response in the telecom bands," *Phys. Rev. B* **108**(8), 085127 (2023).
36. J. Siegel et al., "Rewritable phase-change optical recording in $Ge_2Sb_2Te_5$ films induced by picosecond laser pulses," *Appl. Phys. Lett.* **84**(13), 2250–2252 (2004).
37. C. R. de Galarreta et al., "Nonvolatile reconfigurable phase-change metadevices for beam steering in the near infrared," *Adv. Funct. Mater.* **28**(10), 1704993 (2018).
38. Y. Xie et al., "Self-healing of a confined phase change memory device with a metallic surfactant layer," *Adv. Mater.* **30**(9), 1705587 (2018).
39. P. Hosseini, C. D. Wright, and H. Bhaskaran, "An optoelectronic framework enabled by low-dimensional phase-change films," *Nature* **511**(7508), 206–211 (2014).
40. L. Lu et al., "Inter-diffusion of plasmonic metals and phase change materials," *J. Mater. Sci.* **54**, 2814–2823 (2019).
41. R. Neale and J. A. Aseltine, "The application of amorphous materials to computer memories," *IEEE Trans. Electron Devices* **20**(2), 195–205 (1973).
42. N. Yamada et al., "High speed overwritable phase change optical disk material," *Jpn. J. Appl. Phys.* **26**(S4), 61 (1987).
43. X. Ding et al., "Theoretical analysis and simulation of a tunable mid-infrared filter based on $Ge_2Sb_2Te_5$ (GST) metasurface," *Superlattices Microstruct.* **132**, 106169 (2019).
44. C. Choi et al., "Metasurface with nanostructured $Ge_2Sb_2Te_5$ as a platform for broadband-perating wavefront switch," *Adv. Opt. Mater.* **7**(12), 1900171 (2019).
45. H. Shang et al., "Optical investigation of chalcogenide glass for on-chip integrated devices," *Results Phys.* **28**, 104552 (2021).
46. D. Xia et al., "Integrated chalcogenide photonics for microresonator soliton combs," *Laser Photonics Rev.* **17**(3), 2200219 (2022).
47. D. Xia et al., "Engineered Raman lasing in photonic integrated chalcogenide microresonators," *Laser Photonics Rev.* **16**(4), 2100443 (2022).
48. M. Decker et al., "High-efficiency dielectric Huygens' surfaces," *Adv. Opt. Mater.* **3**(6), 813–820 (2015).
49. X. Wei et al., "Sb_2S_3-based dynamically tuned color filter array via genetic algorithm," *Nanomaterials* **13**(9), 1452 (2023).

Biographies of the authors are not available.